

Anomalous large-angle α -scattering in a single-folding model with microscopic densities

A.-G. Șerban^a, F. Salvat-Pujol^a, and N. Săndulescu^{b*}

^a *European Organization for Nuclear Research,
Esplanade des Particules 1, 1211 Geneva 23, Switzerland*

^b *National Institute of Physics and Nuclear Engineering,
077125 Bucharest-Măgurele, Romania*

P. Marević

*Department of Physics, Faculty of Science,
University of Zagreb, Bijenička c. 32, 10000 Zagreb, Croatia.*

Abstract

We investigate anomalous large-angle scattering (ALAS) of α -particles from $N = Z$ nuclei within the framework of the single-folding model. Differential cross sections are calculated by folding the α -nucleon interaction with nuclear density distributions obtained from both relativistic and non-relativistic mean-field models. The folding procedure employs a Gaussian-form α -nucleon interaction, with its energy dependence and range constrained by previous theoretical studies. Our results show that ALAS in sd -shell nuclei is reasonably well reproduced using the microscopic densities together with an α -nucleon interaction characterized by a unified parameter set, in which only two parameters vary with the mass number.

PACS numbers:

* corresponding author, email: sandulescu@theory.nipne.ro

I. INTRODUCTION

The cross section of low-energy elastic α -particle scattering from several light and medium-mass $N = Z$ nuclei exhibits a pronounced enhancement and an irregular energy dependence at large backward angles (see, *e.g.*, Refs. [1–3] and references therein). These features, which differ from the diffractive behaviour observed at forward angles, are commonly referred to as anomalous large angle scattering (ALAS).

Since ALAS cannot be satisfactorily described within optical models based on a simple Woods-Saxon (WS) potential, a variety of interaction mechanisms have been proposed. These include L -dependent potentials [4], α -exchange processes [5], Regge-pole models [6], and quasi-molecular resonances [7]. Notably, ALAS is predominantly observed in scattering from $N = Z$ nuclei, which are expected to exhibit α -like correlations in their ground states. This observation has motivated interpretations that associate ALAS with scattering between the incident α particle and preformed α clusters within the target nucleus [8–10].

To describe ALAS, modified WS potentials have been also employed as an alternative to the standard optical model (see, *e.g.*, Ref. [2]). While such phenomenological approaches can reproduce the experimental data, they rely on parameters that lack a clear microscopic interpretation. A more physically grounded framework is provided by the single-folding model (see, *e.g.*, Refs. [11, 12]), in which the interaction potential is obtained by folding the α -nucleon interaction with the nuclear density distribution of the target.

Single-folding calculations have led to two main conclusions: (i) the real part of the scattering potential capable of describing ALAS deviates significantly from the standard WS form, and (ii) a satisfactory description of the data requires weak absorption of the incident α particles, typically implemented through an imaginary potential with small strength.

The connection between reduced absorption and ALAS has been discussed in Refs. [13–15]. According to these studies, ALAS arises from those α particles that, owing to weak absorption, penetrate into the target nucleus and are subsequently scattered back by the wall of the effective potential. This interpretation is supported by semiclassical calculations, which show that trajectories entering the nucleus are focused into a single focal point and that a fraction of them re-emerge at backward angles [15].

In most folding calculations addressing ALAS, the real part of the optical potential is obtained by folding the α -nucleon interaction with phenomenological density distributions

of specific functional forms (*e.g.*, modified Gaussian), adjusted to reproduce nuclear root-mean-square radii. Such densities are not expected to provide an accurate description of the density profile throughout the entire nucleus. In the present work, we instead employ realistic nuclear densities derived from self-consistent microscopic mean-field models. An advantage of this approach is that effects related to deformation and ground-state correlations of the target nuclei are naturally incorporated through the density distributions.

In previous studies of α scattering [11, 12], the single-folding model was used to determine only the real part of the optical potential, while the imaginary part was assumed to have a standard WS form. Here, both the real and imaginary parts of the optical potential are derived within the folding framework, using the same microscopic densities and α -nucleon interaction. The latter is assumed to have a Gaussian form with explicit energy and density dependence. To limit the number of free parameters, the energy dependence and range of the real part are fixed according to theoretical estimates [16]. We show that a reasonable description of ALAS in *sd*-shell nuclei can be achieved by allowing only the strengths of the real and imaginary components of the α -nucleon interaction to vary with the mass number.

II. FORMALISM

A. The folding model and the α -nucleon interaction

The differential cross section for elastic scattering of α particle on nuclei is calculated with the following interaction potential between the α particle and the target nucleus:

$$V(r_\alpha) = V_C(r_\alpha) + V_{an}(r_\alpha), \quad (1)$$

where $V_C(r_\alpha)$ and $V_{an}(r_\alpha)$ are, respectively, the electrostatic and nuclear interaction potentials, while r_α is the distance between the point-like α particle and the center of the target nucleus.

The electrostatic potential is taken as the Coulomb interaction between a uniformly charged sphere (the target nucleus) and a point charge (the α particle). Its expression is:

$$V_C(r_\alpha) = \begin{cases} \frac{Z_p Z_t e^2}{2R} \left(3 - \frac{r_\alpha^2}{R^2} \right), & r_\alpha < R, \\ \frac{Z_p Z_t e^2}{r_\alpha}, & r_\alpha \geq R, \end{cases} \quad (2)$$

where $R = 1.3A^{1/3}$ is the radius of the target nucleus with atomic mass A . Z_p and Z_t are the proton numbers of the projectile and of the target nucleus, respectively, and $e^2 = 1.44 \text{ MeV fm}$ is the square of the elementary charge.

The nuclear potential is obtained by folding an effective α -nucleon interaction with the density distribution of the nucleons in the target nucleus (see, *e.g.*, Ref. [17]). Specifically,

$$V_{\alpha n}(r_\alpha) = 4\pi \int v_{\alpha n}(s)\rho(r_n)r_n^2 dr_n, \quad (3)$$

where r_n denotes the coordinate of a nucleon inside the nucleus, $s = |r_\alpha - r_n|$ is the distance between the α particle and the nucleon, ρ is the nuclear density distribution of the target nucleus, and $v_{\alpha n}$ represents the α -nucleon interaction.

Within the single-folding model of Eq. (3), the α -nucleon interaction is taken in the following phenomenological form:

$$v_{\alpha n}(s) = Ve^{-(s/a_R)^2} + iWe^{-(s/a_I)^2}, \quad (4)$$

where V and W are the strengths of the real and the imaginary parts, respectively, and a_R and a_I are their corresponding ranges.

It is worth recalling that the real part of the α -interaction can be also derived via folding model calculations based on nucleon-nucleon interaction [16]. When the antisymmetrization between the nucleons of the target and the nucleons from the α particle is taken into account, the exchange term makes the α -interaction non-local. This non-local interaction can be replaced by a local interaction which depends on the energy. In Ref. [16] it is shown that this energy-dependent interaction can be fitted by

$$v_{eff}(s, E) \approx U_0(1 - \beta E)e^{-(s/a_R)^2}. \quad (5)$$

The parameters derived in [16] for the Brink and Boeker force are $U_0 = -47.3 \text{ MeV}$ and $\beta = 0.003 \text{ MeV}^{-1}$, while $a_R = 1.97 \text{ fm}$. This energy dependence is included in the present calculations.

The effective α -nucleon interaction is also expected to depend on the nuclear matter density in which the nucleons interact. This density dependence is commonly represented in the following form [12, 17]:

$$f(\rho) = 1 - \gamma\rho^{2/3}, \quad (6)$$

where γ is a fitting parameter. In folding calculations, the factor $f(\rho)$ reduces the interaction strength in the interior of the target, where the density is highest, while leaving the surface and asymptotic regions largely unaffected. Such a modification is expected to improve the description of α scattering at large angles [17].

Regarding the imaginary part of the α -nucleon interaction, no fully reliable microscopic derivation is available to guide the construction of an effective interaction appropriate for ALAS studies. For example, a microscopic treatment of the imaginary interaction has been presented in Ref. [18]; however, it relies on approximations that are not valid at the low incident energies relevant for ALAS. For this reason, in the present work we assume that the imaginary part of the α -nucleon interaction exhibits the same functional dependence on energy and density as the real part.

Based on the above considerations, in this work we adopt the following parametrization for the α -nucleon interaction:

$$v_{\alpha n}(s) = g_{\text{R}}f_{\text{R}}(E_{\alpha}, \rho)e^{-(s/a_{\text{R}})^2} + ig_{\text{I}}f_{\text{I}}(E_{\alpha}, \rho)e^{-(s/a_{\text{I}})^2}, \quad (7)$$

where the density ρ is evaluated at the position of the nucleon. The energy and density dependence is taken in the form

$$f_k(E_{\alpha}, \rho) = U_0(1 - \beta E_{\alpha})(1 - \gamma_k \rho^{2/3}), \quad (8)$$

where $k = \text{R, I}$. Since the antisymmetrization effects are expected to influence the real and the imaginary parts in a similar manner, the same parameters U_0 and β are used for both components.

B. The nuclear density

In the folding model [Eq. (3)], we employ target densities obtained from self-consistent relativistic and nonrelativistic mean-field calculations. In the following, we briefly outline the underlying framework of these models and discuss the resulting density distributions relevant for the present study.

B1. Nuclear densities from relativistic mean-field calculations

These densities are computed within the relativistic Hartree-Bogoliubov (RHB) framework [19], which provides a unified description of particle-hole (ph) and pairing correlations. In the present calculations, the ph channel is described using the DD-PC1 energy density functional [20], while pairing correlations are included in the neutron-neutron and proton-proton channels. The latter are treated using a separable Gaussian interaction adjusted to reproduce the pairing gap in nuclear matter obtained with the Gogny D1S force [21, 22].

The RHB equations are solved in a basis of axially symmetric harmonic-oscillator wave functions. In this framework, the intrinsic ground states do not possess well-defined angular momentum and parity. To restore these symmetries, we apply the Generator Coordinate Method (GCM) and perform Hill-Wheeler-type configuration mixing calculations. Specifically, states with good angular momentum and parity are constructed as:

$$|JM\pi; \alpha\rangle = \sum_i \sum_K f_\alpha^{JK\pi}(q_i) P_{MK}^J P^\pi |\phi(q_i)\rangle, \quad (9)$$

where P_{MK}^J and P^π denote the angular-momentum and parity projection operators, respectively. This expression shows that the ground state $|JM\pi; \alpha\rangle$ is a linear combination of projected RHB (proj-HFB) states, $P_{MK}^J P^\pi |\phi(q_i)\rangle$, each built from an intrinsic wave function $|\phi(q_i)\rangle$ characterised by a quadrupole deformation q_i . For convenience, we referred to this wave function as RHB+PGCM. Further details on the RHB+PGCM calculations can be found in Ref. [23].

In Fig. 1, we display the densities obtained from RHB+PGCM calculations for the even $N = Z$ nuclei in the first half of the *sd* shell. All considered nuclei exhibit deformed ground states, with quadrupole deformation parameters $\beta_2 = 0.27, 0.43, \text{ and } -0.38$, respectively. These values are obtained by averaging the contributions of the intrinsic $|\phi(q_i)\rangle$ states of different deformations that are mixed in the RHB+PGCM wave function. The corresponding experimental deformation parameters are 0.72, 0.606, and 0.412, respectively. It should be noted that, for ^{28}Si , experimental data cannot distinguish between prolate and oblate shapes.

For comparison, Fig. 1 also includes the RHB densities calculated under the assumption of spherical symmetry. A pronounced difference between the RHB+PGCM and spherical RHB densities is observed, particularly in the nuclear interior, where the spherical RHB densities are significantly reduced. This behavior can be traced back to the weak pairing correlations

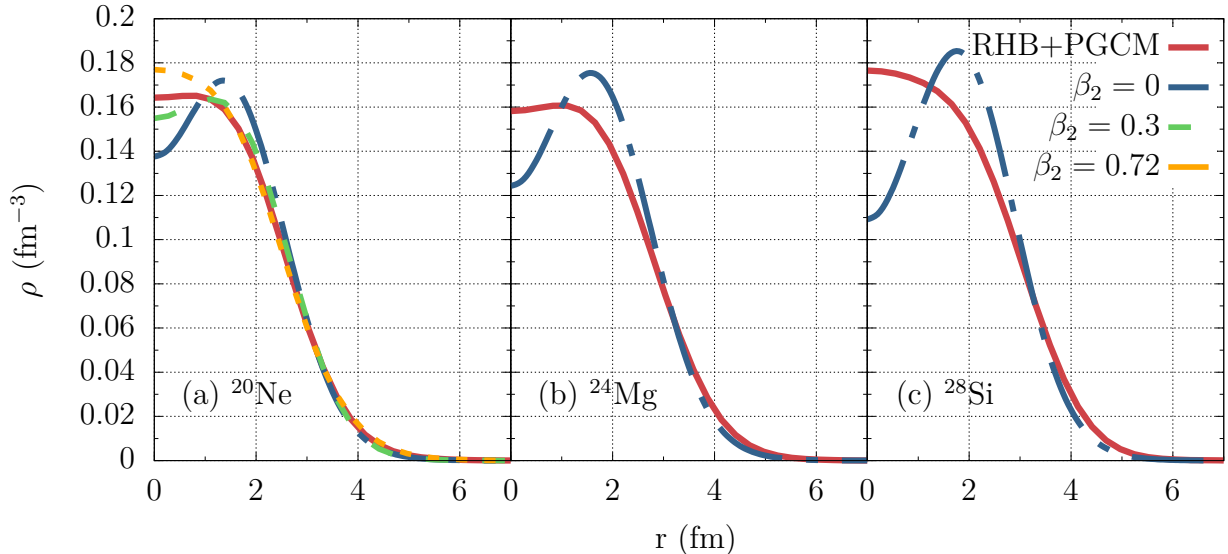


FIG. 1: Nuclear densities of ^{20}Ne , ^{24}Mg , and ^{28}Si calculated within the RHB+PGCM framework and with spherically symmetric RHB solutions ($\beta_2 = 0$). For ^{20}Ne , densities calculated with proj-HFB states corresponding to quadrupole deformations $\beta_2 = 0.3$ and 0.72 are also shown.

in the spherical RHB calculations, which do not lead to a substantial occupation of the $2s_{1/2}$ single-particle orbital — a state that contributes prominently to the central density.

In contrast, in the RHB+PGCM calculations, the occupation of the $2s_{1/2}$ orbital is enhanced due to the proximity of single-particle levels arising from the deformation-induced splitting of the $1d_{5/2}$ orbital. This results in an increased central density. To further illustrate the impact of deformation on the interior density, Fig. 1 also shows, for ^{20}Ne , the densities provided by the proj-HFB states corresponding to the deformations $\beta_2 = 0.3$ and 0.72 .

B2. Nuclear densities from non-relativistic mean field calculations

The non-relativistic mean field is described with the quark-meson coupling (QMC) energy density functional (EDF) [24], which reproduces nuclear properties with an accuracy comparable to, and in some cases exceeding, that of standard Skyrme EDFs, while employing fewer adjustable parameters. In contrast to conventional mean-field approaches, where nucleons are treated as point-like particles, the QMC model describes nucleons as composite systems of three confined quarks interacting via scalar and vector meson fields. A notable feature of the QMC EDF is that its density dependence arises microscopically, while the

spin-orbit and tensor terms are obtained without introducing additional parameters.

In the present QMC EDF calculations both the isovector ($T = 1$) and isoscalar ($T = 0$) pairing correlations are included and treated within the quartet condensation model (QCM) [25]. In this framework, the ground state of even-even $N = Z$ nuclei is described by the wave function

$$|\text{QCM}\rangle = (Q_{T=1}^\dagger + \Delta_0^{\dagger 2})^{(N+Z)/4}|0\rangle, \quad (10)$$

where $Q_{T=1}^\dagger = 2\Gamma_1^\dagger\Gamma_{-1}^\dagger - (\Gamma_0^\dagger)^2$ is the isovector quartet operator expressed in terms of the collective pair operators. The latter are defined by $\Gamma_t^\dagger = \sum_i x_i P_{i,t}^\dagger$, where $P_{i,t}^\dagger$ creates an isovector pair in the time-reversed states (i, \bar{i}) . The isoscalar pairing correlations are described by the collective isoscalar pair $\Delta_0^\dagger = \sum_i y_i D_{i,0}^\dagger$, where $D_{i,0}^\dagger = (\nu_i^\dagger \pi_i^\dagger - \pi_i^\dagger \nu_i^\dagger)/\sqrt{2}$. Finally, $n_q = (N + Z)/4$, where N and Z are the number of neutrons and protons above the core $|0\rangle$ which are considered in the pairing calculations. In the present QCM calculation we take $n_q = 3$ (for details, see Ref. [26]).

The QCM wave function exhibits several distinctive features compared to the RHB+PGCM state discussed above [Eq. (9)]. Specifically: (i) it includes not only neutron-neutron and proton-proton pairing, but also both isovector and isoscalar proton-neutron pairing correlations; (ii) it exactly conserves particle number and isospin, although not angular momentum; and (iii) it incorporates four-body correlations induced by the pairing interaction.

The QCM calculations are done with the following isovector pairing interaction, derived within the QMC framework [24]

$$V_P^{(T=1)}(\mathbf{r}, \mathbf{r}') = -sV_0 \left(1 - \eta \frac{\rho(\mathbf{r})}{1 + d'G_\sigma\rho(\mathbf{r})} \right) \delta(\mathbf{r} - \mathbf{r}'), \quad (11)$$

where ρ is the baryon density, $V_0 = G_\sigma - G_\omega - G_\rho/4$ and $\eta = d'G_\sigma^2/V_0$. The interaction depends on the coupling constants for the scalar, vector and isovector mesons, $G_i = g_i^2/m_i^2$, and on $d' = d + G_\sigma\lambda_3/3$, where d is the nuclear polarizability and λ_3 is associated with the cubic term of the σ field. For these parameters we employ the values provided in Ref. [24]. Finally, s is a scaling factor chosen to improve the description of odd-even mass differences for $N > Z$ nuclei (for details, see Ref. [26])

For the isoscalar channel, the pairing interaction is assumed to be proportional to the isovector one,

$$V_P^{(T=0)} = wV_P^{(T=1)}, \quad (12)$$

with $w = 1.6$. This value lies in the range for which the Gamow-Teller strength for ^{56}Ni , which depends only on the $T = 0$ pairing, is reasonably reproduced [27].

The ground states of even-even $N = Z$ nuclei are determined by performing axially deformed QMC+QCM calculations, following the procedure outlined in Ref. [26]. From the resulting axially symmetric densities, spherical densities are constructed by averaging over the polar angle,

$$\rho(r) = \frac{1}{2} \int_0^\pi \rho(r, \theta) \sin \theta d\theta. \quad (13)$$

This procedure provides an approximate restoration of spherical symmetry for the densities. A more rigorous approach would involve angular-momentum projection, as employed in the RHB+PGCM calculations discussed in the previous subsection. However, such a method is not currently available within the QMC+QCM framework.

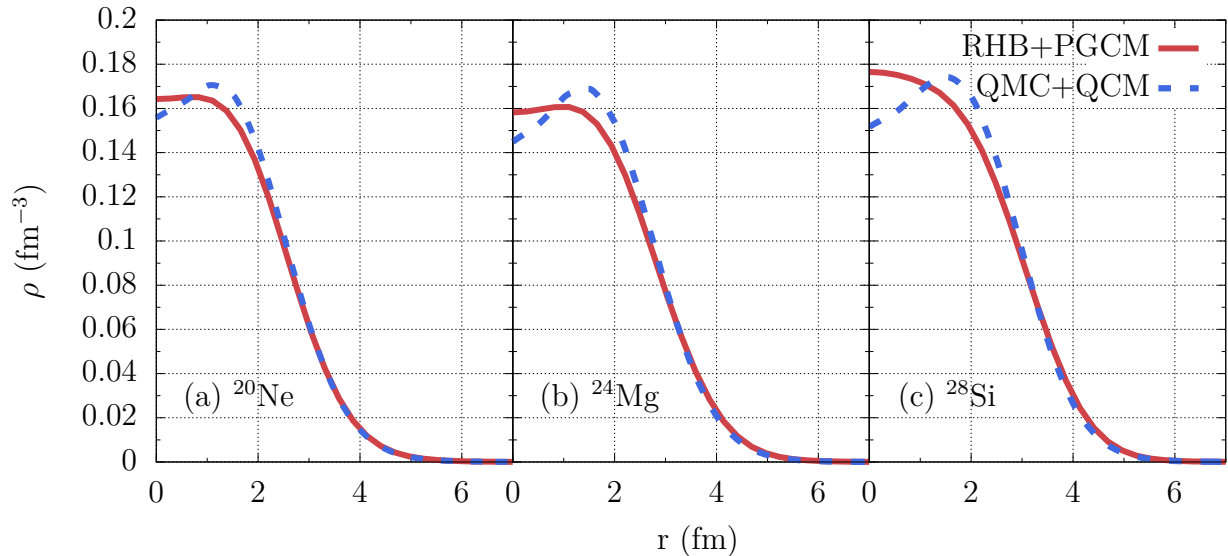


FIG. 2: Nuclear densities of ^{20}Ne , ^{24}Mg , and ^{28}Si calculated within the QMC+QCM approach, compared with the RHB+PGCM densities.

Fig. 2 shows the densities obtained from the QMC+QCM calculations for ^{20}Ne , ^{24}Mg , and ^{28}Si , whose intrinsic quadrupole deformations are 0.474, 0.478, and -0.308 , respectively. The corresponding RHB+PGCM densities are also included in the figure for comparison. It can be observed that the QMC+QCM densities are lower in the central region and larger at radial distances between approximately 1 and 2–3 fm. This behavior is mainly due to the reduced occupation of the $2s_{1/2}$ orbital in the QMC+QCM approach compared to

RHB+PGCM, which in turn enhances the population of deformed states originating from the $1d_{5/2}$ orbital. These states are more localized at finite radii inside the nucleus, leading to a depletion of the central density and an enhancement in the region $r \approx 1 - 3$ fm.

As a general conclusion, the densities in the nuclear interior exhibit a strong sensitivity to the choice of mean field, pairing interaction, and its treatment. However, this sensitivity is significantly reduced in the surface and tail regions, which are expected to play the dominant role in the low-energy α -scattering processes analyzed in this work.

C. Evaluation of the α -particle elastic differential cross section

The differential cross section has been evaluated with the nuclear potential provided by Eq. (3). The latter has been obtained by numerical integration in spherical coordinates. The calculation has been optimized by assuming the z -axis aligned with the distance r_α between the α particle and the target nucleus. With this choice, the dependence on the azimuthal angle φ is eliminated. The nuclear potential can then be written as

$$V_{\alpha n}(r_\alpha) = 2\pi \int_0^{R_{\text{nuc}}} \int_0^\pi \rho(r_n) v_{\alpha n}(s) r_n^2 \sin \theta dr_n d\theta, \quad (14)$$

where s denotes the distance between the α particle and the nucleon,

$$s = \sqrt{r_\alpha^2 + r_n^2 + 2r_\alpha r_n \cos \theta}. \quad (15)$$

With the total nuclear and the electrostatic potential we solve the radial Schrödinger equation:

$$-\frac{\hbar^2}{2\mu} \frac{d^2 P_{E\ell}(r)}{dr^2} + \left[\frac{\hbar^2 \ell(\ell+1)}{2\mu r^2} + V(r) \right] P_{E\ell}(r) = E P_{E\ell}(r), \quad (16)$$

where ℓ is the orbital angular momentum, and μ is the reduced mass

$$\mu = \frac{m_\alpha m_t}{m_\alpha + m_t}, \quad (17)$$

with m_α and m_t denoting the masses of the α particle and the target nucleus, respectively. The Schrödinger equation has been solved numerically using the RADIAL Fortran subroutine package [28] and the phase shift δ_ℓ was derived for each orbital angular momentum ℓ .

Finally, the differential cross section for the elastic scattering of an α particle along a direction $\hat{\Omega} = (\theta, \varphi)$ with respect to the incident direction, is expressed as:

$$\frac{d\sigma}{d\hat{\Omega}} = |f(\hat{\Omega})|^2, \quad (18)$$

where the scattering amplitude has the standard expression

$$f(\hat{\Omega}) = \frac{1}{2ik} \sum_{\ell=0}^{\infty} (2\ell + 1) P_{\ell}(\cos \theta) (e^{2i\delta_{\ell}} - 1). \quad (19)$$

In this expression, k represents the center-of-mass wavevector, and $P_{\ell}(\cos \theta)$ are the Legendre polynomials.

D. Calculation scheme and fitting procedure

The differential cross section (DCS) depends on the inputs used in the folding calculations, namely the nuclear densities and the α -nucleon interaction. The parameters of the α -nucleon interaction are determined through the fitting procedure described below. In this procedure, we employ nuclear densities obtained from the RHB+PGCM calculations described above. This choice is motivated by the fact that, within the RHB+PGCM framework, spherical symmetry is properly restored through angular-momentum projection.

To reduce the number of free parameters, the energy-dependent factor of the α -nucleon interaction is taken from the theoretical estimates of Ref. [16]. In addition, the range of the real part is fixed at $a_{\text{R}} = 2$ fm, which is close to the value $a_{\text{R}} = 1.97$ fm considered in Ref. [16].

TABLE I: Minimum and maximum values of each parameter, together with the corresponding number of evaluation points, used in the initial coarse fitting step.

Parameter	g_{R}	g_{I}	a_{I} (fm)	γ_{R} (fm ²)	γ_{I} (fm ²)
Min.	0.1	0.01	1.9	1.7	1.7
Max.	3.5	1.0	2.3	2.1	2.1
N_p	8	7	9	5	5

The rest of the parameters have been determined through a fitting procedure as follows. For each pair of target nucleus and α -particle energy considered in this work, the fit parameters have been varied initially on a coarse grid, as displayed in Table I. Then, the interaction potential, Eq. (1), has been evaluated for each combination of fit parameters. Next, the DCS has been calculated for each evaluated interaction potential, as discussed in the foregoing section.

Nucleus	E_α (MeV)	$g_R \pm \sigma_{g_R}$	$g_I \pm \sigma_{g_I}$	Cor(g_R, g_I)	Nucleus	E_α (MeV)	$g_R \pm \sigma_{g_R}$	$g_I \pm \sigma_{g_I}$	Cor(g_R, g_I)
^{20}Ne	33.00	2.7 ± 0.26	0.30 ± 0.21	-0.34	^{40}Ar	22.10	2.0 ± 0.037	0.20 ± 0.026	-0.213
	50.90	2.0 ± 0.71	0.45 ± 0.26	0.54		24.10	2.1 ± 0.097	0.20 ± 0.063	-0.216
	54.10	2.1 ± 0.68	0.50 ± 0.30	0.53		29.20	1.9 ± 0.192	0.25 ± 0.116	-0.275
	104.00	2.7 ± 0.93	0.80 ± 0.30	0.84		104.00	2.1 ± 0.108	0.70 ± 0.046	0.702
^{24}Mg	22.10	2.0 ± 0.068	0.15 ± 0.004	0.34	^{40}Ca	22.00	2.1 ± 0.648	0.10 ± 0.0029	0.90
	39.00	2.7 ± 0.036	0.30 ± 0.019	0.014		24.10	2.1 ± 0.094	0.10 ± 0.0098	0.91
	50.00	2.7 ± 0.086	0.45 ± 0.016	0.068		29.00	2.2 ± 0.052	0.15 ± 0.0053	0.03
	119.70	1.5 ± 0.060	0.50 ± 0.029	0.90		104.00	1.5 ± 0.815	0.45 ± 0.0228	0.79
^{28}Si	40.00	1.8 ± 0.064	0.25 ± 0.023	-0.20	^{44}Ca	22.00	1.8 ± 0.033	0.15 ± 0.0129	0.496
	45.00	1.3 ± 0.054	0.30 ± 0.017	0.34		24.10	1.9 ± 0.022	0.15 ± 0.0109	0.806
	50.00	2.3 ± 0.062	0.35 ± 0.015	0.24		29.00	2.2 ± 0.023	0.20 ± 0.0199	0.556
	104.00	2.2 ± 0.079	0.60 ± 0.023	0.77		104.00	1.4 ± 0.050	0.50 ± 0.0244	0.747
^{36}Ar	17.50	2.2 ± 0.020	0.09 ± 0.002	0.061	^{48}Ca	22.00	2.1 ± 0.051	0.15 ± 0.0264	0.473
	22.10	2.2 ± 0.032	0.15 ± 0.010	0.002		24.10	2.1 ± 0.041	0.15 ± 0.0073	-0.146
	24.10	2.2 ± 0.041	0.15 ± 0.014	0.455		29.00	1.7 ± 0.016	0.15 ± 0.0099	0.788
	29.20	1.9 ± 0.016	0.15 ± 0.007	0.448		104.00	2.1 ± 0.060	0.60 ± 0.0193	0.790

TABLE II: Fit parameters, their standard deviations σ , and their correlation coefficients, for the target nuclei and α -particle energies considered in this work.

To maximize the agreement between the distorted-wave and the experimental DCS, the following measure has been adopted:

$$\chi^2 = \sum_{i=1}^N \left(\log \frac{d\sigma(\theta_i)}{d\sigma_R} \Big|_{\text{DW}} - \log \frac{d\sigma(\theta_i)}{d\sigma_R} \Big|_{\text{exp}} \right)^2, \quad (20)$$

where $\frac{d\sigma(\theta_i)}{d\sigma_R} \Big|_{\text{DW}}$ is the distorted-wave DCS at scattering angle θ_i , $\frac{d\sigma(\theta_i)}{d\sigma_R} \Big|_{\text{exp}}$ is the experimental DCS [29, 30] at θ_i , both expressed as a ratio to the Rutherford DCS, and N is the number of experimental CM scattering angles. The combination of fit parameters which minimizes Eq. (20) is searched. Once this is found, the fitting procedure is restarted, employing a refined grid around the best found fit parameters.

Following the procedure described above, the parameters $a_I = 2.25$ fm, $\gamma_R = 1.8$ fm², and $\gamma_I = 1.7$ fm² were found to provide a good description for all the nuclei and all α -particle energies considered in this work. Thus, the only remaining energy- and nucleus-dependent

parameters are the renormalization factors g_R and g_I of the strengths of the real and of the imaginary parts, respectively, of the α -nucleon interaction. These are reported in Table II, along with their correlation coefficient and their standard deviations, which were calculated using the covariance matrix, as explained in the Appendix.

III. RESULTS AND DISCUSSIONS

A. Differential cross sections with RHB+PGCM densities

The main results for the DCSs are presented in Fig. 3, which compares partial-wave DCSs obtained with the single-folding potential (solid red curves) to those calculated using a standard global optical model (OPM) [31] (dashed blue curves) for selected target nuclei and α -particle energies. Experimental angular distributions [29, 30] are shown as black dots. The single-folding results are computed using the α -nucleon interaction specified above and nuclear densities provided by the RHB+PGCM calculations.

As shown in Fig. 3, at low energies — where ALAS is typically observed — the global OPM significantly underestimates the experimental DCS at intermediate and large scattering angles. In contrast, the single-folding calculations reproduce the pronounced backscattering features observed in the data. Moreover, as seen from Fig. 3, the same set of parameters provides a good description of the DCS at higher scattering energies for all calculated nuclei, with the exception of ^{20}Ne .

The large differences between the DCSs obtained with the global OPM and the single-folding approach are also reflected in the corresponding interaction potentials. As an illustrative example, Fig. 4 shows the interaction potential for the scattering of 33 MeV α particles on ^{20}Ne . While the real parts of the two potentials exhibit similar radial dependence, their depths differ significantly. In contrast, the imaginary parts display pronounced differences both in magnitude and shape. In particular, substantial deviations are observed in the central region as well as in the nuclear surface.

A1. Differential cross sections for neutron-rich nuclei

Experimental angular distributions show that the enhancement at large scattering angles is more pronounced in $N = Z$ nuclei than in neutron-rich systems. This behaviour is evident in Fig. 5, where the experimental DCSs [29, 30] for $^{36,40}\text{Ar}$ and $^{40,44}\text{Ca}$ are presented (black

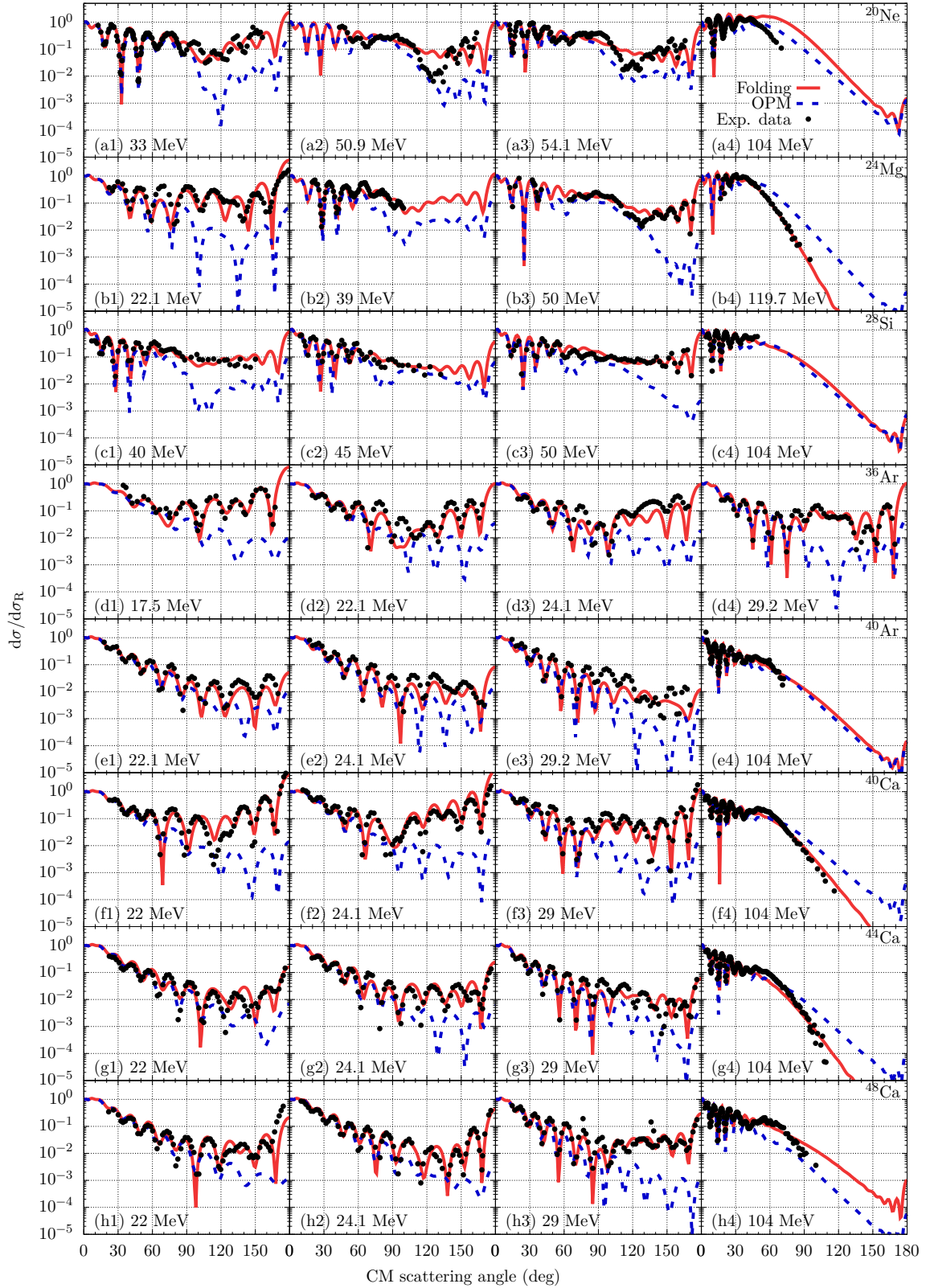


FIG. 3: Comparison of DCSs obtained with the single-folding model employed in this work (solid red curves) and those calculated using a standard global OPM [31] (dashed blue curves), for selected nuclei and α -particle energies. Experimental angular distributions [29, 30] are shown as black dots.

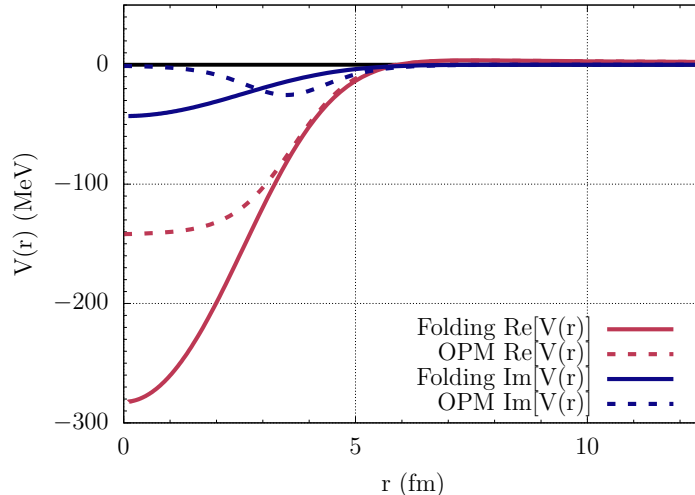


FIG. 4: Interaction potentials (real and imaginary) for the scattering of 33 MeV α particles on ^{20}Ne .

dots). Folding-model calculations based on microscopic densities satisfactorily reproduce the dependence of the large-angle DCS on neutron excess.

In the folding calculations, different values of the parameters g_R and g_I are used for $N = Z$ and $N > Z$ nuclei (Table II). To isolate the effect of density changes associated with the additional neutrons, we evaluate the DCS by interchanging the parameter sets between $N = Z$ and $N > Z$ isotopes. The results for $^{36,40}\text{Ar}$ and $^{40,44}\text{Ca}$ at α -particle energies of 29.2 MeV and 29 MeV, respectively, are shown in Fig. 5. At these energies, g_R is the same for both classes of nuclei (Table II), allowing a more direct assessment of density effects.

A substantial modification of the DCS is observed when the densities of $N = Z$ and $N > Z$ nuclei are interchanged. However, changing only the densities while keeping the imaginary strength g_I fixed does not provide a satisfactory description of the data. For instance, as shown in Fig. 5(b), the DCS for ^{36}Ar cannot be reproduced from that of ^{40}Ar by simply replacing the ^{40}Ar density with that of ^{36}Ar while retaining the g_I value used for ^{40}Ar . A reasonable agreement is achieved only by reducing g_I from 0.25 to 0.15 (Table II).

These results indicate that ALAS in $N = Z$ nuclei cannot be accounted for solely by ground-state density effects. Instead, they point to a significant role of reaction dynamics associated with the excitation spectrum, which is effectively incorporated through the imaginary part of the optical potential.

In fact, the low-energy excitation spectra of ^{36}Ar and ^{40}Ar , which contribute to the inelastic channels included in the imaginary term, differ markedly. In ^{36}Ar , there are only

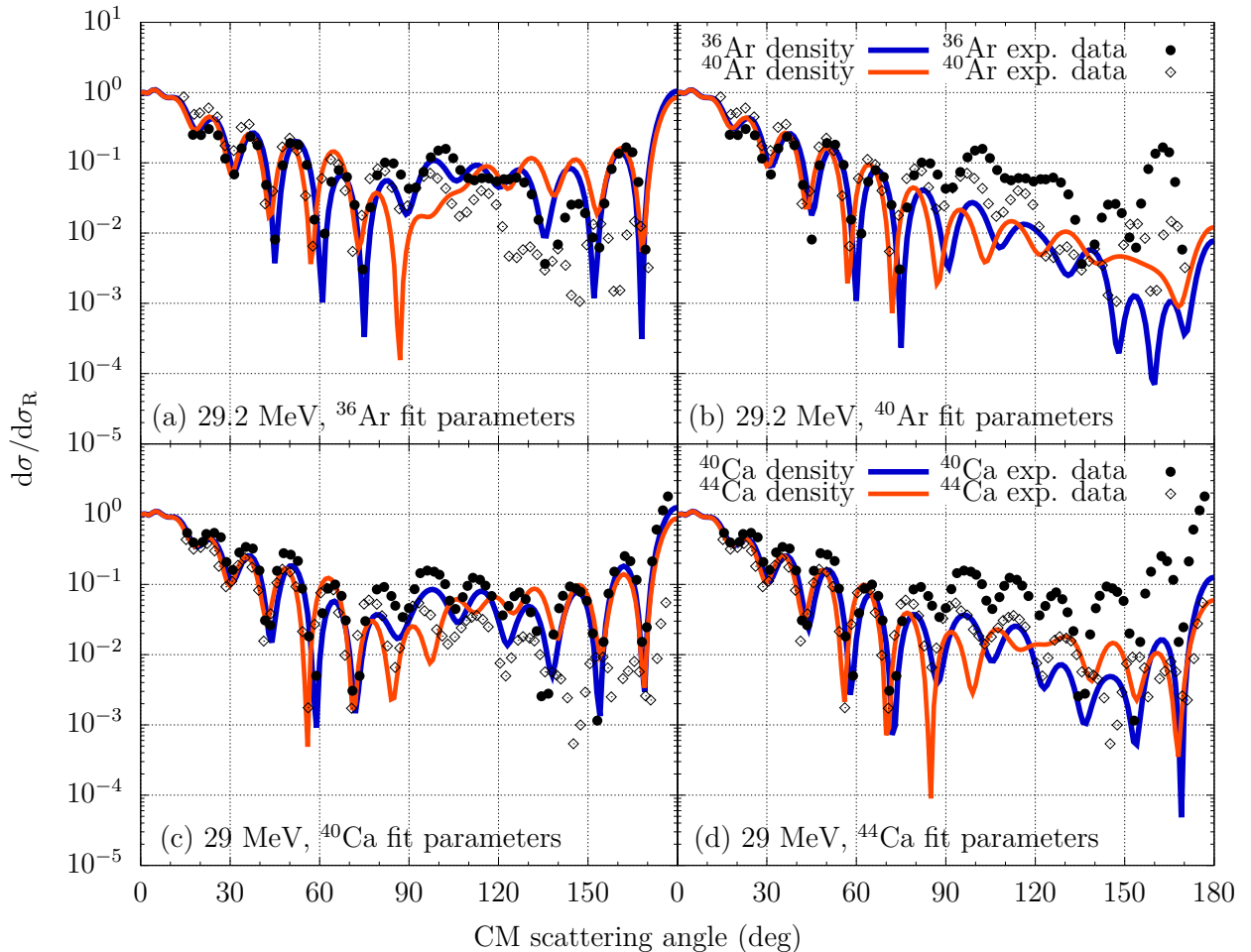


FIG. 5: Cross sections for the elastic scattering of α particles on Ar and Ca isotopes. See text for details.

four excited states below 4.5 MeV: the first at 1.970 MeV, followed by three states above 4 MeV. By contrast, ^{40}Ar exhibits 24 states in the same energy region, with the lowest at 1.460 MeV and three additional states below 3 MeV. This difference in the excitation spectra is consistent with the folding-model results, which require a weaker imaginary potential for ^{36}Ar than for ^{40}Ar .

A2. Effect of nuclear deformations on differential cross sections

Most $N = Z$ nuclei exhibit ground-state deformation. As the density distribution can change significantly with deformation (see, *e.g.*, Fig. 1), a corresponding impact on the DCS is expected. To illustrate this effect, we consider the nucleus ^{20}Ne , which is strongly deformed in its ground state, with $\beta_2 = 0.72$.

Figure 6 shows the DCS calculated for a range of deformations, from the spherical case

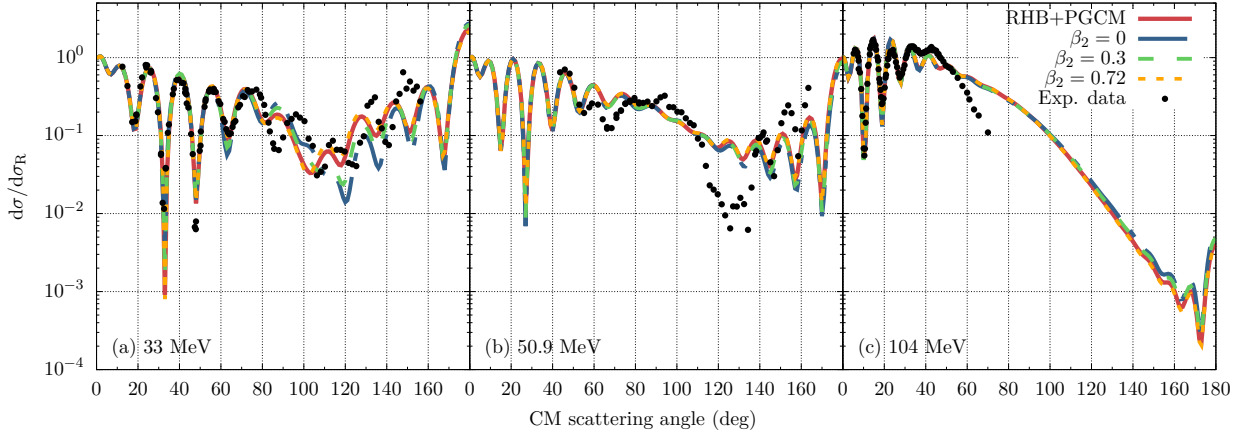


FIG. 6: Effect of deformation in ^{20}Ne on the differential cross section of α -particle at different energies.

up to $\beta_2 = 0.72$. The RHB+PGCM solution corresponds to a mixing of states with different deformation, with an average of $\beta_2 = 0.27$. For low-energy α scattering at 33 MeV, the DCS exhibits a strong dependence on deformation in the angular range 100° - 140° . In particular, at $\theta = 120^\circ$, the DCS increases by nearly an order of magnitude as the deformation changes from $\beta_2 = 0$ to $\beta_2 = 0.72$.

In contrast, at higher scattering energies the sensitivity of the DCS to deformation becomes much weaker. These results indicate that an accurate treatment of nuclear deformation is essential for describing low-energy scattering, where ALAS typically emerges.

B. Differential cross sections with QMC+QCM densities

To compute the DCSs using the QMC+QCM densities, a new set of α -nucleon interaction parameters should, in principle, be determined following the same fitting procedure adopted for the RHB+PGCM densities. However, in order to assess the sensitivity of the DCSs to the choice of nuclear densities employed in the single-folding model, we perform calculations using the parameter set listed in Table II. The most relevant results are presented in Fig. 7.

Overall, the DCSs obtained with the two sets of densities are similar. Although the QMC+QCM densities differ substantially from the RHB+PGCM ones in the nuclear interior (see, *e.g.*, Fig. 2), the corresponding DCSs exhibit only minor variations. This indicates that, in low-energy elastic collisions, the α particle predominantly probes the nuclear surface, where the two density distributions differ only slightly.

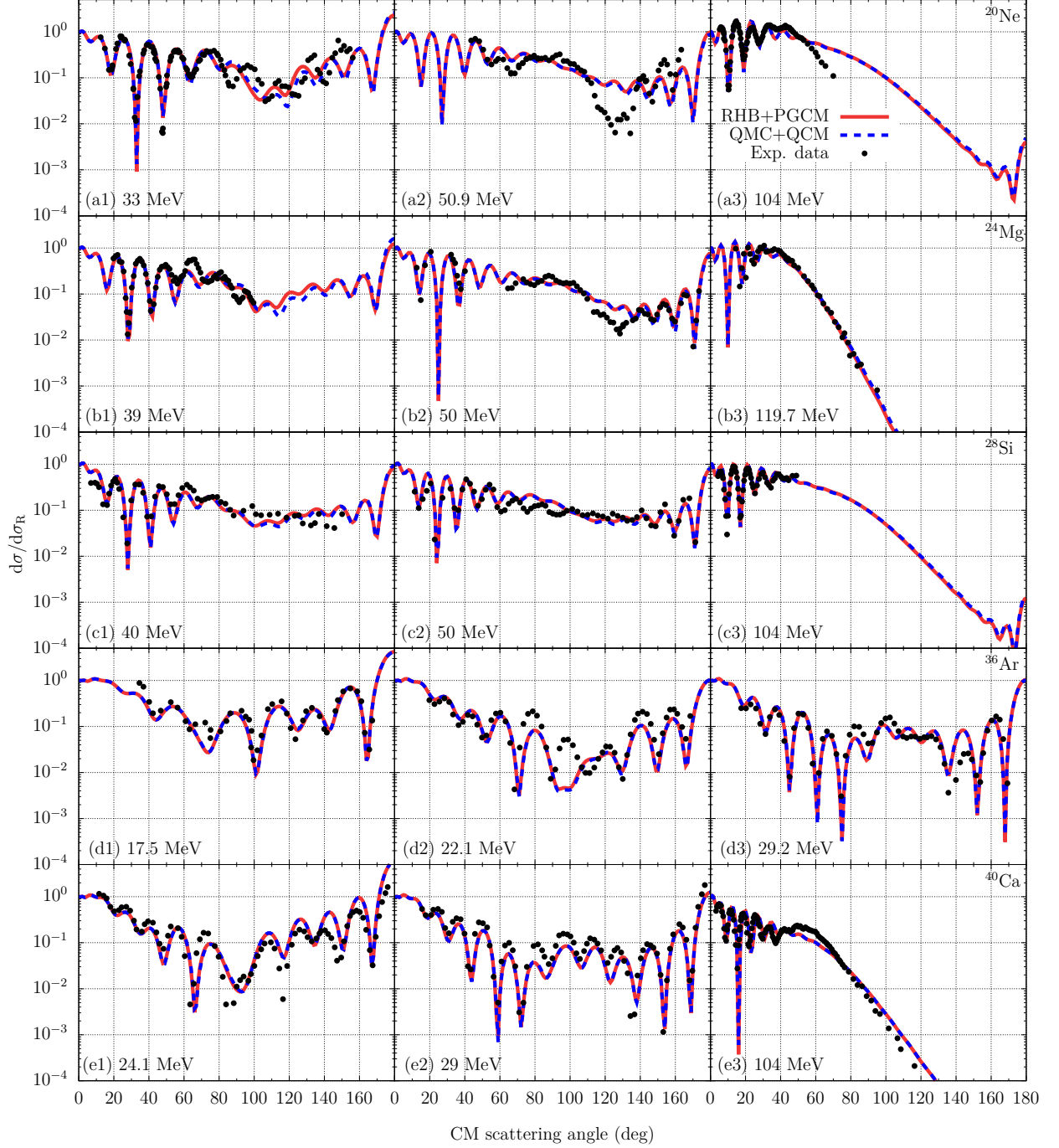


FIG. 7: Differential cross sections calculated with the QMC+QCM densities, compared with results obtained with RHB+PGCM densities. Experimental angular distributions [29, 30] are shown as black dots.

The most noticeable deviations occur for ^{20}Ne at $E_\alpha = 33$ MeV and for ^{24}Mg at $E_\alpha = 39$ MeV, around scattering angles of 120° .

These differences are most likely related to the distinct deformations predicted by the

RHB+PGCM and QMC+QCM approaches. However, a direct comparison between these deformations is not straightforward. In the QMC+QCM framework, the deformation characterizes an axially symmetric intrinsic state, whereas in the RHB+PGCM approach it is associated with a spherically symmetric state constructed as a superposition of intrinsic configurations with different deformations.

The observation that, in some cases, the DCS in the ALAS region is significantly influenced by nuclear deformation (see also Fig. 6) is noteworthy. Since deformation originates from dynamical effects associated with ground-state correlations — such as the interplay between mean-field, pairing and four-body correlations — the DCS in low-energy α scattering on $N = Z$ nuclei in the ALAS region may provide a sensitive probe of these effects. A dedicated investigation of this possibility, however, is beyond the scope of the present work.

IV. SUMMARY AND CONCLUSIONS

In this study, we have shown that a single-folding model based on nuclear densities derived from self-consistent mean-field calculations is able to describe reasonably well the ALAS in even-even sd -shell nuclei. In the present framework, we employ an energy- and density-dependent nucleon- α interaction of Gaussian form for both the real and imaginary components of the scattering potential. The range of the interaction and its energy dependence are constrained by previous theoretical studies. Within this approach, a satisfactory description of the experimental data is achieved using only two adjustable parameters, namely the strengths of the real and imaginary parts of the interaction, g_R and g_I .

Our analysis indicates that, in order to reproduce ALAS, smaller values of g_I are required for $N = Z$ nuclei than for $N > Z$ systems. In particular, we find that simply replacing the density of an $N > Z$ nucleus with that of an $N = Z$ nucleus, without reducing g_I , is insufficient to reproduce ALAS in $N = Z$ nuclei. Since g_I is associated with the effects of inelastic channels, this result suggests that ground-state properties — encoded in the nuclear density — are not, by themselves, sufficient to account for ALAS.

One of the longstanding open questions in ALAS studies is why this phenomenon occurs predominantly in even-even $N = Z$ nuclei and at low scattering energies. An early interpretation attributed ALAS to the scattering of α particles from preformed α clusters assumed to exist at the surface of even-even $N = Z$ nuclei [8–10]. In such approaches, the interaction

is effectively treated as scattering between two α particles, implying that the clusters behave as localized α -like objects. However, this assumption is not supported by microscopic calculations, including the QCM approach employed here. In $N = Z$ nuclei, α -like structures are more appropriately described as four-body correlations in spin and isospin, which are not necessarily spatially localized.

These four-body correlations have a significant impact on binding energies [26, 32] and can also modify the ground-state density. However, as shown in Sec. III B, such modifications do not lead to appreciable changes in the folding-model results. This suggests that ALAS is more closely related to the excitation properties of even-even $N = Z$ nuclei, which are influenced by α -like correlations induced by proton-neutron pairing [33, 34].

More specifically, low-energy excitations in even-even $N = Z$ nuclei require the breaking of four-body correlations (*i.e.*, α -like quartets), followed by the breaking of neutron-neutron, proton-proton, and/or proton-neutron pairs. By contrast, in even-even $N > Z$ nuclei, low-energy excitations predominantly involve pair breaking only. As a consequence, low-energy excitations occur more readily in $N > Z$ nuclei than in $N = Z$ nuclei.

For example, in ^{20}Ne there are only eight excited states below 7 MeV, with the lowest at 1.633 MeV, whereas in ^{22}Ne there are 18 states in the same energy region, with the lowest at 1.274 MeV. A similar trend is observed in the case of ^{36}Ar and ^{40}Ar (see Sec. III A1).

Consequently, the incident low-energy α -particle flux is expected to experience weaker absorption in even-even $N = Z$ nuclei. Within the single-folding model, this reduced absorption — closely related to ALAS [13, 14] — is incorporated phenomenologically through a smaller imaginary component of the α -nucleon interaction in $N = Z$ systems. A fully microscopic description of this mechanism would require evaluating the absorption in terms of the excitation spectra of $N = Z$ nuclei; however, such an approach remains highly challenging and lies beyond the scope of the present work.

Acknowledgments

N. S. acknowledges the support from CERN during his visit related to this study. He also acknowledges the funding from the Romanian Ministry of Education and Research through the project PN-23-21-01-01/2023. The work of P.M. was funded by the European Union’s Horizon Europe research and innovation program under the Marie Skłodowska-Curie Actions Grant Agreement No. 101149053.

APPENDIX

For a model that depends on n parameters, $\mathbf{p} = \{p_1, p_2, \dots, p_n\}$, the best fit parameters, \mathbf{p}_0 , can be found by minimizing

$$\chi^2(\mathbf{p}) = \sum_{i=1}^N (y_i^{\text{exp}} - y_i^{\text{eval}}(\mathbf{p}))^2, \quad (21)$$

where N is the number of experimental data points, y_i^{exp} are the experimental quantities at each experimental data point i , and $y_i^{\text{eval}}(\mathbf{p})$ are the corresponding fitted quantities at each experimental data point i , depending on the fit parameters \mathbf{p} .

After finding the best-fit parameters \mathbf{p}_0 by minimizing $\chi^2(\mathbf{p})$, the covariance matrix of the parameters can be evaluated as [35]:

$$\mathbf{C} = \frac{\chi^2(\mathbf{p}_0)}{N - n} (\mathbf{J}^T \mathbf{J})^{-1}, \quad (22)$$

where $N - n$ is the number of degrees of freedom and \mathbf{J} is the Jacobian matrix, with dimensions $N \times n$. This matrix consists of the first-order derivatives of the residuals, $r_i(\mathbf{p}) = y_i^{\text{exp}} - y_i^{\text{eval}}(\mathbf{p})$, with respect to the parameters:

$$J_{ij} = \frac{\partial r_i(\mathbf{p})}{\partial p_j}. \quad (23)$$

When an explicit analytical form of the derivatives is not available, finite differences can be used to approximate them:

$$J_{ij} = \frac{\partial r_i(\mathbf{p})}{\partial p_j} \approx \frac{r_i(\mathbf{p}_0 + \Delta p_j) - r_i(\mathbf{p}_0)}{\Delta p_j}. \quad (24)$$

Once the covariance matrix \mathbf{C} is known, the correlation coefficient ρ_{ij} between the parameters p_i and p_j is

$$\rho_{ij} = \frac{C_{ij}}{\sqrt{C_{ii}C_{jj}}}, \quad (25)$$

where C_{ij} is the covariance between p_i and p_j , and C_{ii} and C_{jj} are their variances.

The correlation coefficients can take values between -1 and 1 :

- $\rho_{ij} = -1$ indicates a perfect negative correlation, *i.e.*, when one parameter increases, the other decreases.
- $\rho_{ij} = 0$ shows that there is no correlation between the parameters.
- $\rho_{ij} = 1$ indicates a perfect positive correlation, *i.e.*, when one parameter increases, the other increases as well.

-
- [1] G. Gaul *et al.*, Nucl. Phys. A **137**, 177 (1968).
- [2] F. Michel and R. Vanderpoorten, Phys. Rev. C **16**, 142 (1977).
- [3] R. Planeta *et al.*, Nucl. Phys. A **326**, 97 (1979).
- [4] K. A. Eberhard, Phys. Lett. B **33**, 342 (1970).
- [5] D. Agassi and N. S. Wall, Phys. Rev. C **7**, 1368 (1973).
- [6] K. W. McVoy, Phys. Rev. C **3**, 1104 (1971).
- [7] A. S. Rinat, Phys. Lett. B **38**, 281 (1972).
- [8] N. C. Schmeing, Nucl. Phys. A **142**, 449 (1970).
- [9] F. Michel, Phys. Lett. B **60**, 229 (1976).
- [10] Z. M. M. Mahmoud *et al.*, Journ. of Phys. Soc. of Japan **88**,024201 (2019).
- [11] H. P. Gubler *et al.*, Phys. Lett. B **74**, 202 (1978).
- [12] Kassem O. Behairy *et al.*, Nucl. Phys. A **957**, 332 (2017).
- [13] F. Michel, Shigeo and G. Reindemeister, Progr. Theor Phys. Supp. **132**, 7 (1998).
- [14] J. Albinski and F. Michel, Phys. Rev. C **25**, 213 (1982).
- [15] F. Brau, F. Michel and G. Reindemeister, Phys. Rev. C **57**, 1386 (1998).
- [16] M. Lassaut and N. Vinh Mau, Phys. Lett. B **70**, 14 (1977).
- [17] G. R. Satchler, Dao T Khoa, Phys. Rev. C **55**, 285 (1997).
- [18] M. Lassaut and N. Vinh Mau, Nucl. Phys. A **301**, 118 (1982).
- [19] P. Ring, Prog. Part. Nucl. **37**, 193 (1996).
- [20] T. Nikšić, D. Vretenar, and P. Ring, Phys. Rev. C **78**, 034318 (2008).
- [21] T. Duguet, Phys. Rev. C **69**, 054317 (2004).
- [22] Y. Tian, Z. Y. Ma, and P. Ring, Phys. Lett. B **676**, 44 (2009).
- [23] P. Marevic, J-P Ebran, E. Khan, T. Niksic, D. Vretenar, Phys. Rev. C **97**, 024334 (2018).
- [24] K. L. Martinez, A. W. Thomas, P. A.M. Guichon, and J. R. Stone, Phys. Rev. C **102**, 034304 (2020).
- [25] N. Sandulescu, D. Negrea and D. Gambacurta, Phys. Lett. B **751**, 348 (2015).
- [26] T. Popa, N. Sandulescu, and D. Gambacurta, arXiv:2603.25359 (2026).
- [27] H. Sagawa, C. L. Bai, and G. Colo, Phys. Scripta **91**, 083011 (2016).
- [28] F. Salvat and J.M. Fernández-Varea, Comp. Phys. Comm. **240**, 165 (2019).

- [29] N. Otuka *et al.*, Nucl. Data Sheets **120**, 272 (2014).
- [30] V.V. Zerkin and B. Pritychenko, Nucl. Instrum. Meth. A **888**, 31 (2018).
- [31] X.-W. Su and Y.-L. Han, Int. J. Mod. Phys. E **24**, 1550092 (2015).
- [32] D. Negrea, N. Sandulescu and G. Gambacurta, Phys. Rev. C **105**, 034325 (2022).
- [33] M. Sambataro and N. Sandulescu, Phys. Lett. B **820**, 136476 (2021).
- [34] M. Sambataro and N. Sandulescu, Eur. Phys. J. A **59**, 4 (2023).
- [35] M. Kortelainen *et al.*, Phys. Rev. C **82**, 024313 (2010).